Available online at www.sciencedirect.com

ScienceDirect

Ceramics International 40 (2014) 3089–3095

CERAMICS INTERNATIONAL

www.elsevier.com/locate/ceramint

Structural, morphological and up-converting luminescence characteristics of nanocrystalline Y_2O_3:Yb/Er powders obtained *via* spray pyrolysis

V. Lojpur[a], L. Mancic[a,*], P. Vulic[b], M.D. Dramicanin[c], M.E. Rabanal[d], O. Milosevic[a]

[a]*Institute of Technical Sciences of SASA, Belgrade, Serbia*
[b]*Faculty of Mining and Geology, Department of Crystallography, University of Belgrade, Serbia*
[c]*Vinča Institute of Nuclear Sciences, University of Belgrade, Belgrade, Serbia*
[d]*University Carlos III of Madrid, Leganes, Madrid, Spain*

Received 4 September 2013; received in revised form 10 September 2013; accepted 1 October 2013
Available online 8 October 2013

Abstract

Sub-micronic, spherical Y_2O_3:Yb/Er particles comprising clustered nano-units (70 nm) were prepared *via* ultrasonic spray pyrolysis from pure nitrate precursor solutions with different Yb/Er dopant ratios. The particles were additionally thermally treated at 1100 °C for 12, 24 and 48 h. The structural and morphological characteristics of particles were studied by X-ray powder diffraction, Fourier transform infrared spectroscopy, field-emission scanning electron microscopy, energy dispersive X-ray analysis and specific surface area (BET) and were further correlated with their advanced optical properties. For the recorded up-conversion emissions, originating from the following Er^{3+} transitions: [$^2H_{9/2}\rightarrow{}^4I_{15/2}$] in blue (407–420 nm); [$^2H_{11/2}$, $^4S_{3/2}\rightarrow{}^4I_{15/2}$] green: 510–590 nm; and [$^4F_{9/2}\rightarrow{}^4I_{15/2}$] in red (640–720 nm) spectral region, the corresponding lifetimes were acquired in the wide temperature range (10–300 K). The most intense green up-conversion emission with the long decay of 550 ms is recorded for $Y_{1.97}Yb_{0.02}Er_{0.01}O_3$ particles thermally treated at 1100 °C for 24 h.

Keywords: Up-converter; Y_2O_3:Yb/Er; Luminescence; Decay time; Spray pyrolysis

1. Introduction

Rare earth (RE)-doped nanocrystalline materials are of particular importance since they have proven to be efficient up- and down-converters with potential use in screen displays, fluorescent labels for detection of bio-molecules, security marks, lasers, temperature sensors, solar cells, etc. [1,2] RE^{3+} ions doped in the host matrix can serve either as activators or sensitizers since their optical properties depend on the configuration of the 4f inner shell, which is partly filled with electrons. All configurations have different energies, giving rise to energy levels in the ultraviolet, visible and (near) infra-red spectrum ranges. Up-conversion is defined as the anti-Stokes process where two or more photons with a smaller energy are 'added up' to obtain one photon with a high energy [3]. In the case of Yb^{3+}- and Er^{3+}-doped up-converters, Yb^{3+} ion, as a sensitizer, enhances the absorption at 980 nm and transfers this energy further to excite higher energy levels of Er^{3+}. This is due to the fact that the absorption coefficient of Yb^{3+} around this wavelength is at least ten times higher than that of Er^{3+} [4]. The up-conversion process starts with the initialization of the $^2F_{5/2}\rightarrow{}^2F_{7/2}$ transition in Yb^{3+}. The absorbed energy is then transferred to Er^{3+}, which is raised to the $^4I_{11/2}$ excited state. The second energy transfer step from Yb^{3+} raises Er^{3+} to the $^4F_{7/2}$ level and after the relaxation to the $^4S_{3/2}$ level the characteristic green $^4S_{3/2}\rightarrow{}^4I_{15/2}$ emission around 550 nm is observed [5]. It is well known that the overall up-conversion depends on several processes which may occur after absorption. It has been pointed out that the type of the host matrix and the particle size are also are important factors that affect luminescence [6]. Although alkaline-earth fluoride crystals have been considered as one of the most efficient upconversion host with a phonon energy below 500 cm^{-1}, rare-earth sesquioxides have some advantages when chemical stability and thermal

*Corresponding author. Tel.: +381 11 2636994; fax: +381 11 2185263.
E-mail addresses: lidija.mancic@itn.sanu.ac.rs, lidma@yahoo.com (L. Mancic).
URL: http://itn.sanu.ac.rs/lidijamancic_en.htm (L. Mancic).

0272-8842/$ - see front matter © 2013 Elsevier Ltd and Techna Group S.r.l. All rights reserved.
http://dx.doi.org/10.1016/j.ceramint.2013.10.002

conductivity are of importance. The high concentration of defects at the surface of nanoparticles generally leads to decreased luminescence [7] but it has also been demonstrated that spherically assembled nanoparticles, synthesized by solvothermal method, exhibits the same or improved optical properties, compared to commercial ones [8]. We have so far synthesized a variety of submicronic RE^{3+}-doped nanocrystalline down-converting Y_2O_3, $(Y_{1-x}Gd_x)_2O_3$ and Gd_2O_3 spherical particles with advanced structural, morphological and luminescent properties using the spray pyrolysis method [9–12]. We have demonstrated that improved luminescence properties are associated with the nanostructural nature of un-agglomerated particles with a narrow size distribution and a homogenous distribution of dopants in the host matrix [12]. Aiming to investigate the morphology aspect of upconverting nanocrystalline particles, we have recently studied droplet-to-particle formation mechanisms in $Y_{1.89}Yb_{0.1}Er_{0.01}O_3$ dispersed system [13,14], as well as the low-temperature sensitivity and structural properties of Y_2O_3:Yb^{3+}/Tm^{3+} and Y_2O_3:Yb^{3+}/Ho^{3+} sub-micronic particles synthesized by spray pyrolysis [15]. Here, the effect of different Yb^{3+} content on up-conversion characteristic in Yb^{3+}- and Er^{3+}- co-doped Y_2O_3 powders ($Y_{1.97}Yb_{0.02}Er_{0.01}O_3$ and $Y_{1.94}Yb_{0.05}Er_{0.01}O_3$) generated by spray pyrolysis was for the first time monitored in a wide temperature range (from 10 to 300 K) and it was correlated with the structural and morphological properties of powders.

2. Experimental

2.1. Materials

Stoichiometric amounts of $Y(NO_3)_3 \cdot 6H_2O$, $Yb(NO_3)_3 \cdot 5H_2O$ and $Er(NO_3)_3 \cdot 5H_2O$ (p.a. Sigma Aldrich) were carefully measured and dissolved in Millipore's Lab Water in order to obtain 0.1 mol/dm^3 precursor solutions with different Yb/Er ratios. The synthesis of $Y_{1.97}Yb_{0.02}Er_{0.01}O_3$ (Yb/Er=2) and $Y_{1.94}Yb_{0.05}Er_{0.01}O_3$ (Yb/Er=5) powders included the atomization of the precursor solution at 1.3 MHz (RBI, France) and aerosol decomposition in the air stream. A high-temperature tubular reactor with three temperature zones (500/900/900 °C) was used to ensure continuous drying of droplets, precipitation and precursor decomposition for the residence time of about 20 s. The powders obtained were additionally annealed at 1100 °C under steady-state conditions for 12, 24 and 48 h.

2.2. Characterization methods

An X-ray powder diffraction analysis (XRPD) was performed on Rigaku Ultima IV diffractometer operating with a Cu Kα radiation at 40 mA and 40 kV, in the 2θ range from 10° to 100° using the step scan of 0.02 and the counting time of 10 s per step. A Rietveld structural refinement was done in the Topas Academic 4.1 software [16]. In order to determine the microstructural parameters, the Fundamental Parameter Approach was used; the FWHM-based LVol (volume weighted mean column height) calculation used to determine the intermediate crystallite size broadening was modeled by a Voigt function. The shape of the particles and their chemical purity were investigated by means of field-emission scanning electron microscopy (FESEM) coupled with energy dispersive X-ray (EDAX) analysis (HITACHI SU-70). The particle specific surface area was determined by the BET method, while particle size distribution was analyzed by laser particle sizer (Mastersizer 2000, Malvern Instruments). The infrared absorption spectra (FT-IR) were recorded in the range of 4000–400 cm^{-1} on a Nicolet spectrophotometer (Model 380, Thermo Nicolet Corporation, Madison, USA) in the powders freestanding form (not in KBr pellets). The photoluminescence emission spectra and decay time measurements were performed on a spectroflurometer system comprising an optical parametric oscillator excitation source (EKSPLA NT 342, emission range 210–2300 nm), Cryostat (Advance Research Systems DE202-AE) equipped with Lakeshore model 331 controller, a spectrograph FHR 1000 (Horiba Jobin-Yvon, 300 groove/mm grating) and an ICCD detector (Horiba Jobin-Yvon 3771).

3. Results and discussion

3.1. The morphological and chemical characterization of the powders

The typical morphology of the Yb^{3+}- and Er^{3+}- co-doped Y_2O_3 particles obtained by spray pyrolysis is presented in Fig. 1. During spray pyrolysis, the nucleation, growth and collision of primary nanoparticles occur within the small, confined volume of droplets, resulting in the generation of spherical, un-agglomerated sub-micronic particles presented in Fig. 1. The composite substructure of spherical particles becomes more apparent after an additional thermal treatment of powders. Primary particles, around 70 nm in size, representing either crystallites or block-mosaic assembles, coalesce entirely into small secondary particles or densify with the existing nanoporosity into bigger ones thereby providing a large surface area. The secondary particle size distribution in the as-prepared (asp) powder accumulated around 950 nm (inset in Fig. 1a) slightly changed with the increased annealing time up to 12 h, and then rose to 1.2 and 1.8 μm (after 24 and 48 h of annealing) due to interparticle sintering (see supplement file). The high particle reactivity and intensive mass transport at elevated temperatures result in significant broadening of the particle size distribution after 48 h of annealing (d_{90}=3.4 mm). The observed behavior is confirmed by the significant decrease of the particle specific surface from 3 m^2/g in as-prepared powders to 2 (12 h), and further to 0.3 m^2/g, after 24 and 48 h of annealing. The uniform compositional distribution of the constitutive elements (Y, Yb and O) inside the sub-micronic spherical particles obtained *via* spray pyrolysis was confirmed by EDAX performed in the selected area, Fig. 2. Erbium was not detected due to the sensitivity limits of the analysis applied, but its presence was verified by the luminescence measurement. High particle purity was confirmed by a FT-IR analysis. The typical spectrum, Fig. 3, shows sharp peaks at 560 cm^{-1} and 462 cm^{-1}

assigned to the Y–O bond vibrations. It is noticeable that there is no sign either of residual NO_3^- (at 1410–340 and 860–800 cm^{-1}) or OH^- (at 1650 and 3400 cm^{-1}) and CO_3^{2-} groups (around 1500 cm^{-1}), which may quench emission by intensifying non-radiative relaxation [9]. The peak at 2350 cm^{-1} is due to CO_2 physically adsorbed from the measurement environment.

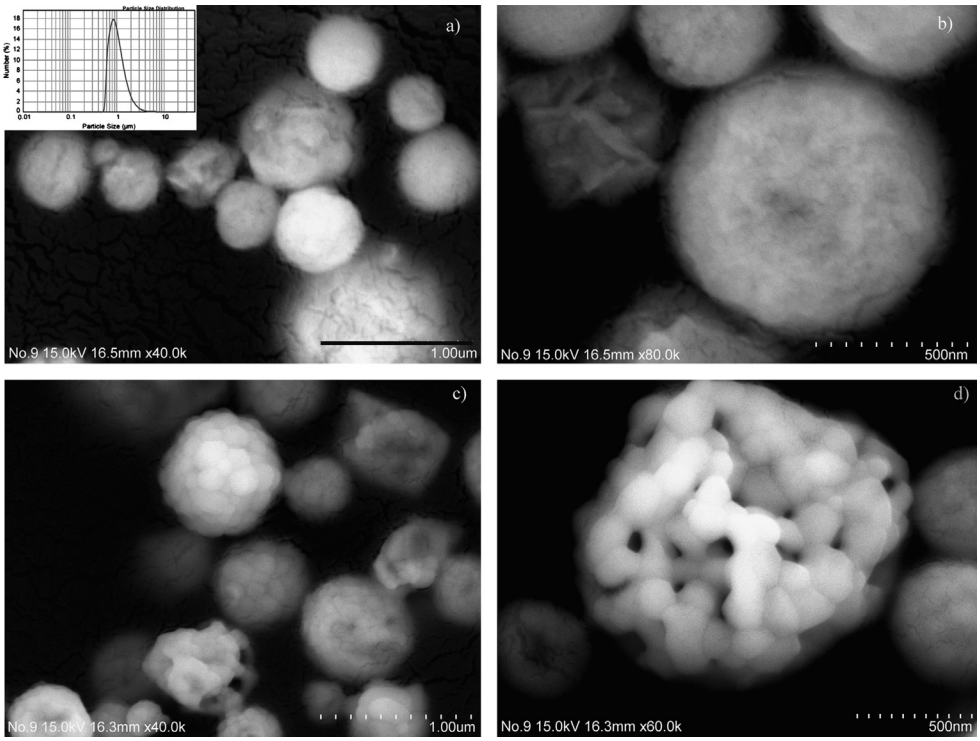

Fig. 1. FESEM micrographs of as-prepared $Y_{1.94}Yb_{0.05}Er_{0.01}O_3$ (a,b) and powders heat treated at 1100 °C for 24 h (c,d); The corresponding laser particle size distribution is given as the inset.

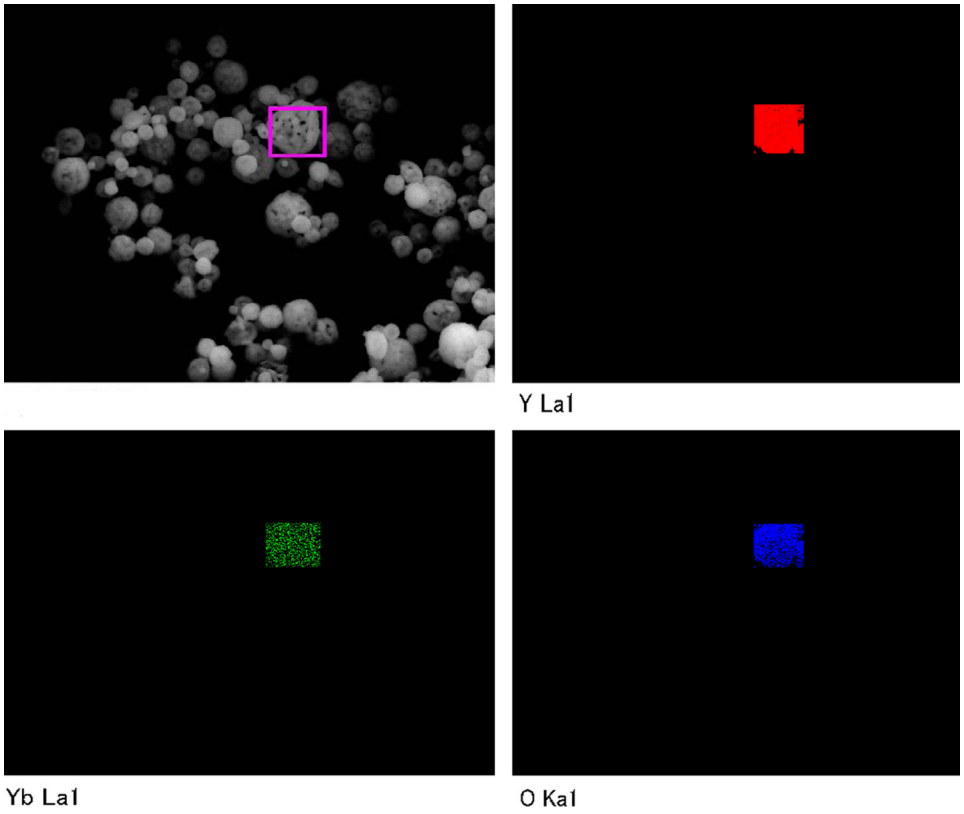

Fig. 2. EDAX of $Y_{1.97}Yb_{0.02}Er_{0.01}O_3$ powders heat treated at 1100 °C for 24 h.

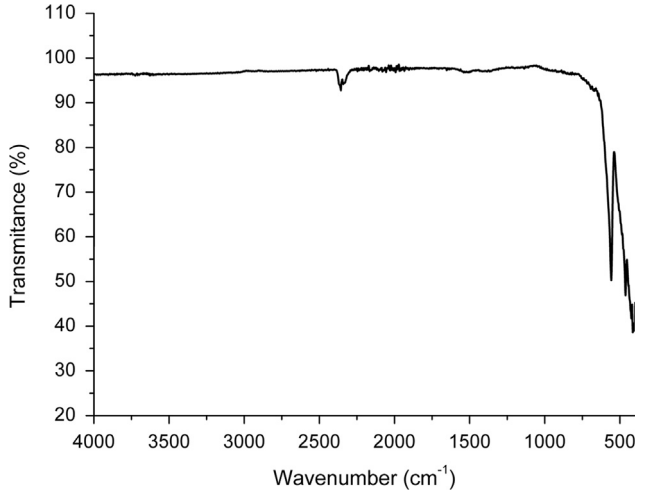

Fig. 3. FTIR of $Y_{1.97}Yb_{0.02}Er_{0.01}O_3$ powders heat treated at 1100 °C for 12 h.

3.2. XRPD and structural refinement

The X-ray powder diffraction analysis has shown that all of the synthesized powders have a cubic bixbyte crystal structure, space group *Ia-3*. The detected peak positions correspond well to those reported for $Y_{1.88}Yb_{0.12}O_3$ (PDF 87-2368). The reflections of thermally treated powders have much narrower peaks which confirm an increased particle crystallinity. A detailed microstructural analysis performed by the Rietveld refinement of the powders thermally treated for 24 h (Table 1, Fig. 4) reveals negligible changes in the crystal cell parameters due to the incorporation of Yb^{3+} and Er^{3+}, compared to the pure Y_2O_3 phase (PDF 89-5591, $a=10.6$ Å). Generally speaking, the Yb^{3+} and Er^{3+} ions could be randomly distributed over two nonequivalent crystallographic sites: non-centrosymmetric C_2 at the 24d site and centrosymmetric S_6 (C_{3i}) at the 8a site; or could exhibit a preference for one of this two positions at low dopant concentrations [17]. Since the cation site occupancy is a very important structural parameter which influences luminescence efficiency, the refinement of both positions was performed. The obtained results imply that the substitution of Y^{3+} (with Yb^{3+} and Er^{3+}) is more pronounced in the position C_2 than in the S_6 position (lower values for the C_2 site occupation with Y^{3+} were obtained, Table 1), irrespective of the dopant concentration. The average crystallite size of ~70 nm confirms the nanostructural nature of heat-treated powders and indicates that the primary particles visible at higher SEM magnifications (Fig. 1d) are monocrystals assembled into spherical secondary particles.

3.3. Optical characterization of the powders

The up-conversion luminescence spectra upon excitation at 978 nm for all powders are presented in Fig. 5. The most prominent green luminescence peak is placed at 563 nm, the less intensive red at 660 nm, while the weak blue emission at 407 nm almost diminishes in powders with a lower Yb^{3+} content ($Y_{1.97}Yb_{0.02}Er_{0.01}O_3$). With the lowering of the Yb^{3+} content, the intensification of green and weakening of red luminescence is also observed. The sharp emission peaks are assigned to the

Table 1
Refined structural parameters of nanocrystalline $Y_{1.89}Yb_{0.05}Er_{0.01}O_3$ and $Y_{1.89}Yb_{0.02}Er_{0.01}O_3$ powders.

	$Y_{1.89}Yb_{0.05}Er_{0.01}O_3$ 1100 °C – 24 h	$Y_{1.89}Yb_{0.02}Er_{0.01}O_3$ 1100 °C – 24 h
Unit cell parameter, *a* (Å)	10.59915 (6)	10.60199 (6)
Crystallite size (nm)	69 (1)	71 (1)
[a]Y_1:O bond length (Å)	2.216 (4)	2.236 (1)
	2.267 (4)	2.284 (1)
	2.340 (4)	2.348 (1)
[a]Y_2:O bond length (Å)	.283 (4)	2.269 (1)
[a]Y_1(Y^{3+}, Yb^{3+}, Er^{3+}) *x* O^{2-}	−0.0321(1)	−0.0310(1)
x	0.3953(4)	0.3906(1)
y	0.1554 (3)	0.1538 (1)
z	0.3778 (3)	0.3796 (1)
Occ Y_1 with Y^{3+}	0.9693	0.9828
Occ Y_2 with Y^{3+}	0.9721	0.9916
R_{Bragg}	2.69	2.388

[a]Y_1 corresponds to C_2 site; Y_2 corresponds to S_6 site in cubic crystal unit cell, space group *Ia-3*.

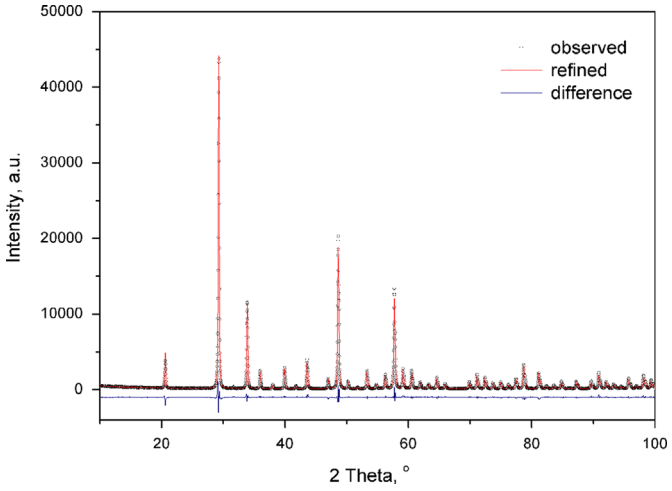

Fig. 4. Rietveld refinement of $Y_{1.94}Yb_{0.05}Er_{0.01}O_3$ annealed at 1100 °C for 24 h.

following Er^{3+} f–f electronic transitions: ($^2H_{11/2}$, $^4S_{3/2}$)→$^4I_{15/2}$ (green: 510–590 nm, two photon process), $^4F_{9/2}$→$^4I_{15/2}$ (red: 640–720 nm, two photon process) and $^2H_{9/2}$→$^4I_{15/2}$ (blue: 407–420 nm, three photon process). Having in mind that Er^+ can be accommodated at two non-equivalent crystallographic sites in Y_2O_3, the different Stark splitting of Er^{3+} 4 f levels may be assumed: the centrosymmetric S_6 site generates the smallest crystal field; accordingly the Er^{3+} ions experience the Stark splitting weaker than 720 cm^{-1}, which occurs on the non-centrosymmetric C_2 site. For the Er^{3+} ions accommodated at the C_2 site, the f–f transitions are partially allowed by the forced electric-dipole transition due to the odd parity terms in the crystal field. On the other hand, for the ions situated in the S_6 sites with an inversion symmetry, only weak magnetic dipole-induced

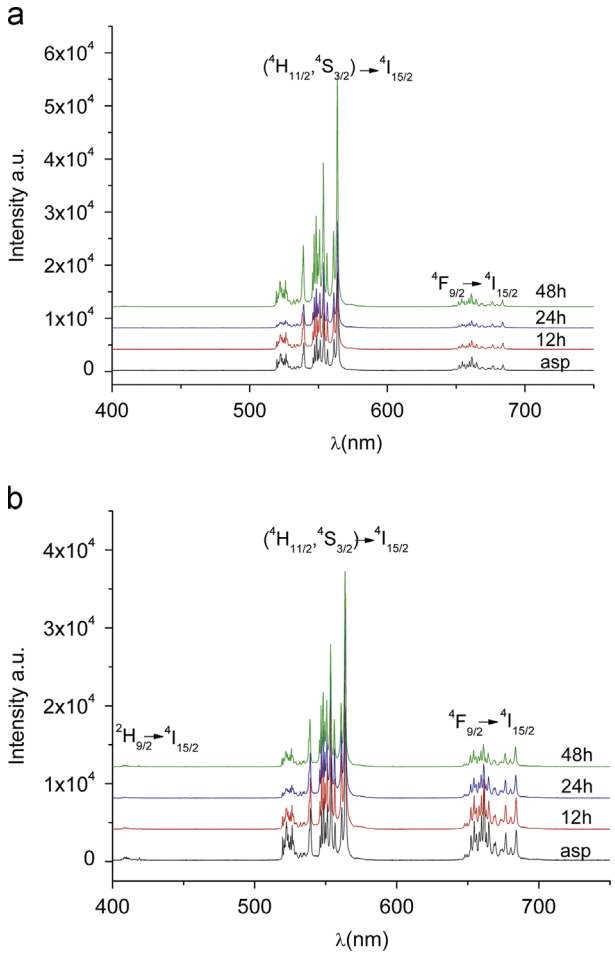

Fig. 5. Up-converted spectra of Er^{3+} in nanocrystalline $Y_{1.97}Yb_{0.02}Er_{0.01}O_3$ (a) and $Y_{1.94}Yb_{0.05}Er_{0.01}O_3$ (b) powders excited at 978 nm.

transitions are possible. Therefore, the 4f spectra presented in Fig. 6 are related to the electric dipole transitions from the Er^{3+} ions accommodated at the C_2 sites and the magnetic dipole transitions originating from both sites. The detailed description of the different competitive paths, presented in Fig. 6, which follow the energy transfer from Yb^{3+} to Er^{3+} and generate the corresponding up-conversion, is as follow: populating the $^4F_{7/2}$ level in Er^{3+} leads to an intermediate non-radiative relaxation to the $^2H_{11/2}$ and $^4S_{3/2}$ levels, and, further, to two partially overlapping green emissions at 522 and 563 nm due to the radiative relaxations to the $^4I_{15/2}$ level. Alternatively, the $^4F_{7/2}$ level may partially non-radiatively relax to the $^4F_{9/2}$ level, giving rise to red emission at 660 nm ($^4F_{9/2} \rightarrow ^4I_{15/2}$). Red emission can be intensified by another up-conversion path which occurs after a non-radiative relaxation of the $^4I_{11/2}$ to the $^4I_{13/2}$ level, whence the additional population of the $^4F_{9/2}$ level occurs through energy transfer. The population of the $^2H_{9/2}$ level is accomplished by the excited state absorption from the $^4I_{13/2}$ and $^4F_{9/2}$ levels. Blue up-conversion emission occurs by its radiative de-excitations to the $^4I_{15/2}$ level. The described emission bands mostly correspond to Er^{3+} on the C_2 site, whose occupation is more pronounced in both systems, as it has been shown by XRPD structural refinement (Table 1). The fact that a prolonged heat treatment is accompanied by an increased intensity of green emission and decreased intensities of other types of emission are

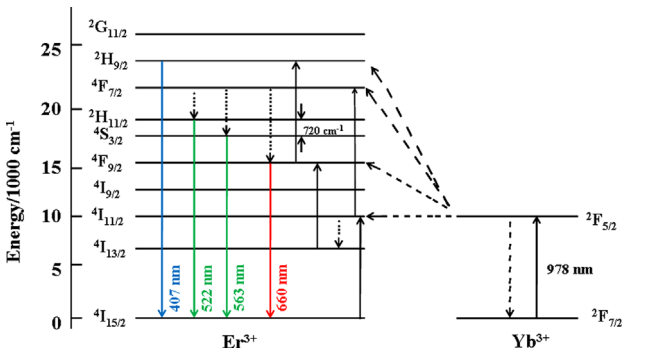

Fig. 6. Energy level diagrams of Yb^{3+} and Er^{3+} ions following excitation with 978 nm.

reflected in the ordering of the host lattice and the consequent alteration of the cross relaxation processes in nanocrystalline particles [18]. The decay times of the nanocrystalline $Y_{1.97}Yb_{0.02}Er_{0.01}O_3$ and $Y_{1.94}Yb_{0.05}Er_{0.01}O_3$ powders were acquired upon excitation at 978 nm at room temperature and they are presented in Table 2 for blue, green and red emissions. In all cases, the decays are extrapolated with a single-exponential function. As it was expected, the lowest values of the emission decay times were detected in the as-prepared samples. This is due to the fact that the applied processing parameters during spray pyrolysis ensure high heating and cooling rates in droplet/particles, so the as-prepared powders are characterized with the lower crystallinity and higher defect concentration [15]. With a heat treatment prolonged up to 24 h, all emission decay times increase. Further prolonging of the thermal treatment results in shorter emission decay times. This could be associated with the slightly increased mean particle sizes due to interparticle sintering at longer annealing times. In all of the samples, the red emission decay times have the highest values. Although it is difficult to compare the presented results with the literature data due to the fact that the most of the results given for the Yb/Er ratios investigated in our study are not accompanied by the same compound stoichiometry, the decay times obtained here differ from the literature data at least by one order of magnitude [19,20]. Such a long emission period implies a very good up-conversion efficiency of the powders [21]. The best decay time values have been observed in the powders heat treated for 24 h (blue – 240 ms, green – 550 ms, red – 670 ms). Accordingly, the temperature-dependent up-conversion emission and the corresponding decay times for these powders were also recorded. In order to enable an easy tracking of temperature-related changes between the red and green emission intensities, the ratios of their integrated areas *R*/*G* (*R*, red: 640–720 nm and *G*, green: 510–590 nm) vs. temperature are presented in Fig. 7. They show that the green emission is dominant throughout the temperature range investigated in this study. The decrease of the *R*/*G* ratio with the rise of temperature is more pronounced in the powder with a higher ytterbium content ($Y_{1.94}Yb_{0.05}Er_{0.01}O_3$), but lower *R*/*G* values (i.e. stronger green emission) are detected in the nanocrystalline $Y_{1.97}Yb_{0.02}Er_{0.01}O_3$ powder. The temperature dependence of the $^2H_{11/2} \rightarrow ^4I_{15/2}$ green emission is assumed to be related to the thermalization process between the $^4S_{3/2}$ and $^2H_{11/2}$ levels, separated by an energy gap of about 720 cm^{-1}, presented at Fig. 6. Namely, when two energy levels in activator ion (in this

Table 2
The decay times of nanocrystalline $Y_{1.97}Yb_{0.02}Er_{0.01}O_3$ and $Y_{1.94}Yb_{0.05}Er_{0.01}O_3$ powders upon excitation.

	Decay time (ms)		
	$^2H_{9/2} \rightarrow {}^4I_{15/2}$ Blue (407 nm)	$^2H_{11/2}$, $^4S_{3/2} \rightarrow {}^4I_{15/2}$ Green (563 nm)	$^4F_{9/2} \rightarrow {}^4I_{15/2}$ Red (660 nm)
$Y_{1.97}Yb_{0.02}Er_{0.01}O_3$			
asp	/	0,42	0,47
12 h	0,22	0,50	0,66
24 h	**0,24**	**0,55**	**0,67**
48 h	0,26	0,51	0,48
$Y_{1.94}Yb_{0.05}Er_{0.01}O_3$			
asp	0,11	0,27	0,36
12 h	0,21	0,40	0,53
24 h	**0,22**	**0,48**	**0,58**
48 h	0,20	0,34	0,40

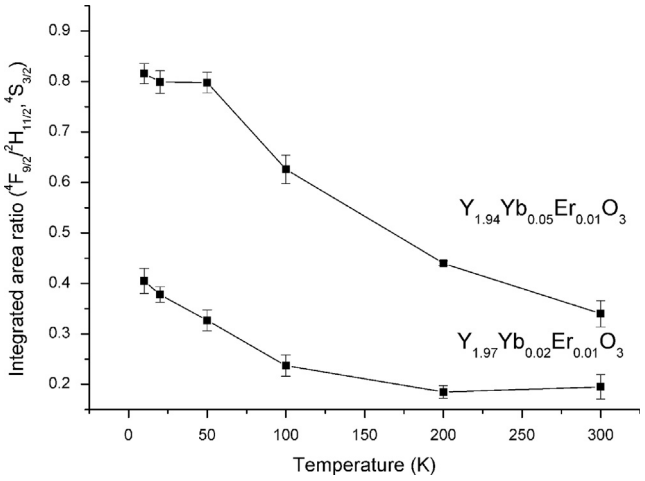

Fig. 7. The temperature dependence of the red to green emission integrated the area ratio of nanocrystalline $Y_{1.97}Yb_{0.02}Er_{0.01}O_3$ and $Y_{1.94}Yb_{0.05}Er_{0.01}O_3$ powders thermally treated for 24 h.

case Er^{3+}) are closely separated by a difference of approximately 1000 cm^{-1}, the upper level does not emit energy at low temperatures due to the high multi-phonon relaxation which quenches it [22]. With the temperature increase, the upper level becomes more populated and, therefore, the emission from this level gradually increases at the expense of the lower level population. The corresponding decay times for blue, green and red emissions acquired in the temperature range from 10 to 300 K are given in Table 3. With temperature decrease, the decay curves change their rates deviating from exponentiality; accordingly, instead of single, double linear interpolation is used to obtain more precise data (see Supplement file). Rather long emissions and the extent of the observed changes in the investigated temperature range will be explored further since this material has a potential use in thermal sensing.

4. Conclusion

In conclusion, we have observed blue, green and red up-conversion emission from nanocrystalline Yb/Er co-doped Y_2O_3 particles synthesized by spray pyrolysis at 900 °C. The Yb^{3+} concentration, crystallinity and the distribution of active ions in the host material affect the final up-conversion efficiency. The most intense green up-conversion emission with a decay time of 550 ms occurs in the $Y_{1.97}Yb_{0.02}Er_{0.01}O_3$ powders thermally treated at 1100 °C for 24 h, having the crystallite size of ~70 nm and the mean particle size of ~950 nm. The long emission lifetimes are the consequence of the achieved purity of the materials, homogeneous doping and the particle composite structure, i.e. persistence of nano-building units in the annealed samples. The rather narrow particle size distribution, the spherical geometry of particles and their un-agglomerated state make them attractive for the manufacturing of display panels, while the observed emission temperature dependence indicates that they also may be used for temperature sensing. Additionally, their composite substructure makes them suitable for the functionalization and surface modification towards more specific application in bioimaging.

Table 3
The temperature dependence of decay times in nanocrystalline $Y_{1.97}Yb_{0.02}Er_{0.01}O_3$ and $Y_{1.94}Yb_{0.05}Er_{0.01}O_3$ powders thermally treated for 24 h (λ_{exc}=978 nm).

	Decay time (ms)		
	$^2H_{9/2} \rightarrow {}^4I_{15/2}$ Blue (418 nm)	$^2H_{11/2}$, $^4S_{3/2} \rightarrow {}^4I_{15/2}$ Green (564 nm)	$^4F_{9/2} \rightarrow {}^4I_{15/2}$ Red (684 nm)
$Y_{1.97}Yb_{0.02}Er_{0.01}O_3$ (K)			
10	τ_1=0.08 τ_2=0.23	0,60	τ_1=0.26 τ_2=0.82
20	τ_1=0.07 τ_2=0.18	0,60	τ_1=0.29 τ_2=0.86
50	τ_1=0.08 τ_2=0.17	0,55	τ_1=0.24 τ_2=0.75
100	τ_1=0.09 τ_2=0.22	0,52	τ_1=0.34 τ_2=0.72
200	0,22	0,55	0,69
300	0,24	0,55	0,67
$Y_{1.94}Yb_{0.05}Er_{0.01}O_3$ (K)			
10	τ_1=0.04 τ_2=0.14	τ_1=0.25 τ_2=0.57	τ_1=0.17 τ_2=0.68
20	τ_1=0.05 τ_2=0.15	τ_1=0.23 τ_2=0.57	τ_1=0.20 τ_2=0.66
50	τ_1=0.05 τ_2=0.14	τ_1=0.23 τ_2=0.48	τ_1=0.19 τ_2=0.62
100	τ_1=0.07 τ_2=0.14	τ_1=0.20 τ_2=0.43	τ_1=0.17 τ_2=0.58
200	τ_1=0.11 τ_2=0.17	0.47	τ_1=0.30 τ_2=0.64
300	0.22	0.48	0,58

Acknowledgment

The financial support for this work was provided by the Ministry of Education and Science of the Republic of Serbia, Project no. 172035.

Appendix A. Supplementary materials

Supplementary data associated with this article can be found in the online version at http://dx.doi.org/10.1016/j.ceramint.2013.10.002.

References

[1] N.O. Nunez, M. Quintanilla, E. Cantelar, F. Cusso, M. Ocana, Uniform YF_3:Yb,Er up-conversion nanophosphors of various morphologies

synthesized in polyol media through an ionic liquid, Journal of Nanoparticle Research 12 (2010) 2553–2565.
[2] V.K. Tikhomirov, V.D. Rodrıguez, J. Mendez-Ramos, J. del-Castillo, D. Kirilenko, G. VanTendeloo, V.V. Moshchalkov, Optimizing Er/Yb ratio and contentin Er–Yb co-doped glass-ceramics for enhancement of the up- and down- conversion luminescence, Solar Energy Materials and Solar Cells 100 (2012) 209–215, http://dx.doi.org/10.1016/j.solmat.2012.01.019.
[3] F. Auzel, Upconversion and anti-stokes processes with f and d ions in solids, Chemical Reviews 104 (2004) 139–173.
[4] A.S.S. de Camarago, L.A.O. Nunes, J.F. Silva, A.C.F.M. Costa, B.S. Barros, J.E.C. Silva, G.F. de Sa, S. Alves Jr., Efficient green and red upconversion emissions in Er^{3+}/Yb^{3+} co-doped $ZnAl_2O_4$ phosphor obtained by combustion reaction, Journal of Physics: Condensed Matter 19 (2007) 246209.
[5] I. Hyppänen, Frequency-Domain and Wide-Pulse Time-Domain measurements of lanthanide luminescence and lanthanide-Based resonance energy Transfer, Dissertation, University of Turku, 2012.
[6] A.M. Pires, S. Heer, H.U. Güdel, O.A. Serra, Er, Yb doped yttrium based nanosized phosphors: particle size, "host lattice" and doping ion concentration effects on upconversion efficiency, Journal of Fluorescence 16 (3) (2006) 461–469.
[7] D. Vennerberg, Z. Lin, Upconversion nanocrystals: synthesis, properties, assembly and applications, Science of Advanced Materials 3 (2011) 26–40.
[8] H. Guo, Y.M. Qiao, Preparation, characterization, and strong upconversion of monodisperse $Y_2O_3:Er^{3+},Yb^{3+}$ microspheres, Optical Materials 31 (2009) 583–589.
[9] M.E. Rabanal, C. Morales, J.M. Torralba, L. Mancic, O. Milosevic, $Gd_2O_3:Eu^{3+}$ phosphor particles processed through aerosol route, Journal of the European Ceramic Society, 25, 2005, p. 2023–2027.
[10] K. Marinkovic, L. Mancic, L.S. Gomez, M.E. Rabanal, M. Dramicanin, O. Milosevic, Photoluminescent properties of nanostructured $Y_2O_3:Eu^{3+}$ powders obtained through aerosol synthesis, Optical Materials, 32, 2010, p. 1606–1611.
[11] L. Mancic, B.A. Marinkovic, K. Marinkovic, M. Dramicanin, O. Milosevic, Soft chemistry routes for synthesis of rare earth oxide nanoparticles with well defined morphological and structural characteristics, Journal of Nanoparticle Research 13 (11) (2011) 5887–5897, http://dx.doi.org/10.1007/s11051-010-0215-9.
[12] O. Milosevic, L. Mancic, M.E. Rabanal, L.S. Gomez, K. Marinkovic, Aerosol route in processing of nanostructured functional materials, KONA 27 (2009) 84–106.
[13] I. Dugandžić, V. Lojpur, L. Mancic, M.D. Dramićanin, M.E. Rabanal, T. Hashishin, Z. Tan, S. Ohara, O. Milošević, Aerosol route as a feasible bottom-up chemical approach for upconverting phosphor particles processing, Advanced Powder Technology 24 (2013) 852–857.
[14] V. Lojpur, L. Mancic, M.E. Rabanal, M.D. Dramicanin, Z. Tan, T. Hashishin, S. Ohara, O. Milosevic, Structural, morphological and luminescence properties of nanocrystalline up-converting $Y_{1.89}Yb_{0.1}Er_{0.01}O_3$ phosphor particles synthesized through aerosol route, Journal of Alloys and Compounds 580 (2013) 584–591.
[15] V. Lojpur, M. Nikolic, L. Mancic, O. Milosevic, M. Dramicanin, Y_2O_3: Yb,Tm and Y_2O_3:Yb,Ho powders for low-temperature thermometry based on up-conversion fluorescence, Ceramics International 39 (2) (2013) 1129–1134.
[16] A.A Coelho, Topas–Academic, 2006.
[17] A. Kremenovic, J. Blanusa, B. Antic, Ph. Colomban, V. Kahlenberg, C. Jovalekic, J. Dukic, A Y_2O_3:Yb nanoscale magnet obtained by HEBM: C_{3i}/C_2 site occupancies, size/strain analysis and crystal field levels of Yb^{3+} ions, Nanotechnology 18 (2007) 145616–145626.
[18] J. Silver, M.I. Martinez-Rubio, T.G. Ireland, G.R. Fern, R. Withnall, The effect of particle morphology and crystallite size on the upconversion luminescence properties of erbium and ytterbium co-doped yttrium oxide phosphors, Journal of Physical Chemistry B 105 (2001) 948–953.
[19] A. Martínez, J. Morales, L.A. Díaz-Torres, P. Salas, E. De la Rosa, J. Oliva, H. Desirena, Green and red upconverted emission of hydrothermal synthesized Y_2O_3: Er^{3+}–Yb^{3+} nanophosphors using different solvent ratio conditions, Materials Science and Engineering: B 174 (2010) 164–168.
[20] F. Vetrone, J.-C. Boyer, J.A. Capobianco, A. Speghini, M. Bettinelli, Significance of Yb^{3+} concentration on the upconversion mechanisms in codoped Y2O3:Er^{3+}, Yb^{3+} nanocrystals, Journal of Applied Physics 96 (2004) 661–667.
[21] X.X. Luo, W.H. Cao, Blue green, red upconversion luminescence and optical characteristics of rare earth doped rare earth oxide and oxysulfide, Science in China Series B: Chemistry 50 (4) (2007) 505–513.
[22] A.H. Khalid, K. Kontis, Thermographic phosphors for high temperature measurements: principles, current state of the art and recent applications, Sensors 8 (2008) 5673–5744.